

11. L. Landau, *Phys. Sov. Union* **2**, 46 (1932).
 12. C. Zener, *Proc. R. Soc. London Ser. A* **137**, 696 (1932).
 13. J. K. Furdyna, *J. Appl. Phys.* **64**, R29 (1988).
 14. M. König *et al.*, *Phys. Rev. Lett.* **96**, 076804 (2006).
 15. T. Koga, Y. Sekine, J. Nitta, *Phys. Rev. B* **74**, 041302(R) (2006).
 16. M. V. Berry, *Proc. R. Soc. London Ser. A* **392**, 45 (1984).
 17. B. A. Piot *et al.*, *Phys. Rev. B* **82**, 081307 (2010).
 18. Materials and methods are available as supplementary materials on *Science Online*.
 19. F. J. Teran *et al.*, *Phys. Rev. Lett.* **88**, 186803 (2002).
 20. M. Cardona, N. E. Christensen, G. Fasol, *Phys. Rev. B* **38**, 1806 (1988).
 21. P. H. Beton *et al.*, *Phys. Rev. B* **42**, 9689 (1990).
 22. C. Jia, J. Berakdar, *Phys. Rev. B* **81**, 052406 (2010).
 23. M. Calvo, *Phys. Rev. B* **18**, 5073 (1978).
 24. O. Zaitsev, D. Frustaglia, K. Richter, *Phys. Rev. B* **72**, 155325 (2005).
 25. M. Popp, D. Frustaglia, K. Richter, *Phys. Rev. B* **68**, 041303(R) (2003).
 26. J. P. Davis, P. Pechukas, *J. Chem. Phys.* **64**, 3129 (1976).
 27. H. Ohno *et al.*, *Nature* **408**, 944 (2000).

Acknowledgments: We thank M. Wimmer for useful discussions and providing the code for the transport equation solver; M. Kiessling for SQUID measurements; M. Wiater for technical assistance in molecular beam epitaxy growth; and C. Back, G. E. W. Bauer, J. Fabian, V. I. Falco, C. Strunk, and G. Woltersdorf for fruitful discussions. We acknowledge financial support from the Deutsche

Forschungsgemeinschaft through SFB 689, WE 247618, FOR 1483, and Elitenetzwerk Bayern. Our research in Poland (V.K., G.K., T.W.) was partially supported by the European Union within the European Regional Development Fund, through Innovative Economy grant POIG.01.01.02-00-008/08.

Supplementary Materials

www.sciencemag.org/cgi/content/full/337/6092/324/DC1
 Materials and Methods
 Supplementary Text
 Figs. S1 to S8
 Table S1
 References (28–39)

1 March 2012; accepted 14 June 2012
 10.1126/science.1221350

A Paramagnetic Bonding Mechanism for Diatomics in Strong Magnetic Fields

Kai K. Lange,¹ E. I. Tellgren,¹ M. R. Hoffmann,^{1,2} T. Helgaker^{1*}

Elementary chemistry distinguishes two kinds of strong bonds between atoms in molecules: the covalent bond, where bonding arises from valence electron pairs shared between neighboring atoms, and the ionic bond, where transfer of electrons from one atom to another leads to Coulombic attraction between the resulting ions. We present a third, distinct bonding mechanism: perpendicular paramagnetic bonding, generated by the stabilization of antibonding orbitals in their perpendicular orientation relative to an external magnetic field. In strong fields such as those present in the atmospheres of white dwarfs (on the order of 10^5 teslas) and other stellar objects, our calculations suggest that this mechanism underlies the strong bonding of H_2 in the $^3\Sigma_u^+(1\sigma_g 1\sigma_u^*)$ triplet state and of He_2 in the $^1\Sigma_g^+(1\sigma_g^2 1\sigma_u^{*2})$ singlet state, as well as their preferred perpendicular orientation in the external field.

Chemical bonding mechanisms are not only well understood phenomenologically and theoretically, but are also accurately described by the methods of modern quantum chemistry. Molecular atomization energies, for example, are today routinely calculated to an accuracy of a few kilojoules per mole—the “chemical accuracy” characteristic of modern measurements (1). However, nearly all our knowledge about chemical bonding pertains to Earth-like conditions, where magnetic interactions are weak relative to the Coulomb interactions responsible for bonding. By contrast, in the atmospheres of rapidly rotating compact stellar objects, magnetic fields are orders of magnitude stronger than those that can be generated in laboratories. In particular, some white dwarfs have fields as strong as 10^5 T, and fields up to 10^{10} T exist on neutron stars and magnetars. Under these conditions, magnetism strongly affects the chemistry and physics of molecules, playing a role as important as that of Coulomb interactions (2). To understand this unfamiliar chemistry, we cannot be guided solely by

the behavior of molecules under Earth-like conditions. In the absence of direct measurements and observations, ab initio (as opposed to semi-empirical) quantum mechanical simulations play a crucial role in unraveling the behavior of molecules in strong magnetic fields and may be useful in the interpretation of white dwarf spectra (3, 4).

Over the years, many quantum chemical studies have been performed on one- and two-electron molecules in strong magnetic fields (5). Some of these demonstrate how certain otherwise unbound one-electron molecules become bound in strong fields. Intriguingly, Hartree-Fock calculations by Žaucer and Ažman in 1978 (6) and by Kubo in 2007 (7) suggest that the otherwise dissociative lowest triplet state $^3\Sigma_u^+(1\sigma_g 1\sigma_u^*)$ of H_2 becomes bound in the perpendicular orientation of the molecule relative to the field. The binding has also been noted in simple model calculations and rationalized in terms of van der Waals binding (dispersion) (8) and a shift of electronic charge density toward the molecular center (9). Bearing in mind that the uncorrelated Hartree-Fock model often strongly overestimates the binding energy in the absence of magnetic fields, these findings must be confirmed by more advanced quantum chemical simulations.

Here, we report highly accurate calculations on H_2 in strong magnetic fields, taking advantage

of our recently developed LONDON code, which is capable of treating molecular systems accurately in all field orientations. Our studies not only confirm the bonding of triplet H_2 but also provide an elementary molecular orbital (MO) explanation that involves neither charge displacement nor dispersion: Nonbonding molecular electronic states are stabilized by the reduction of the paramagnetic kinetic energy of antibonding MOs when these are oriented perpendicular to the magnetic field. The generality of the proposed bonding mechanism is confirmed by calculations on He_2 , previously not studied in strong magnetic fields.

To represent the molecular electronic states in magnetic fields, we use the full configuration-interaction (FCI) method [implemented using string-based techniques (10–12)], where the N -electron wave function is expanded linearly in Slater determinants,

$$|FCI\rangle = \sum_n C_n \det|\phi_{p_{1a}}, \phi_{p_{2a}}, \dots, \phi_{p_{Nn}}| \quad (1)$$

whose coefficients C_n are determined by the Rayleigh-Ritz variation principle (13). Each determinant is an antisymmetrized product of N orthonormal spin MOs ϕ_p ; the summation is over all determinants that may be generated from a given set of MOs. The exact solution to the Schrödinger equation is reached in the limit of a complete set of MOs, making it possible to approach this solution in a systematic manner.

The FCI model makes no assumptions about the structure of the electronic system; in particular, it makes no assumptions regarding the dominance of one Slater determinant (assumed in Hartree-Fock and coupled-cluster theories). This model is therefore capable of describing all bonding situations and dissociation processes in an unbiased manner, which is essential when unfamiliar phenomena are studied. Equally important, the FCI model provides a uniform description of different electronic states and is therefore able to describe the complicated evolution of such states that occurs with increasing field strength.

The FCI method is a standard technique of quantum chemistry, often used to benchmark less expensive and less accurate methods, and was previously used by Schmelcher and Cederbaum in their study of H_2 in strong parallel magnetic fields (14). Our FCI implementation differs from

¹Centre for Theoretical and Computational Chemistry, Department of Chemistry, University of Oslo, N-0315 Oslo, Norway.

²Chemistry Department, University of North Dakota, Grand Forks, ND 58202, USA.

*To whom correspondence should be addressed. E-mail: trygve.helgaker@kjemi.uio.no

theirs in being invariant with respect to gauge origin and hence capable of describing all orientations of the molecule in a field equally well. To understand this point, we recall that the kinetic energy operator (including the spin-Zeeman term) in the magnetic field \mathbf{B} is given, in atomic units, by

$$T = \frac{1}{2} \sum_i \pi_i^2 + \mathbf{B} \cdot \sum_i \mathbf{s}_i, \quad (2)$$

$$\pi_i = -i\nabla_i + \frac{1}{2} \mathbf{B} \times (\mathbf{r}_i - \mathbf{O})$$

where i is the imaginary unit, and π_i and \mathbf{s}_i are the kinetic momentum and spin operators of electron i , respectively. The kinetic energy operator depends parametrically on the gauge origin \mathbf{O} , an arbitrary point in space where the field contribution to the operator vanishes. In exact theory, all choices of \mathbf{O} yield the same energy and other properties of the system; in approximate calculations (except in parallel orientations with the gauge origin on the molecular axis), the calculated results depend on \mathbf{O} unless gauge origin

invariance is carefully imposed. For the results to be reliable, it is essential that the calculations be rigorously invariant with respect to gauge origin in all molecular orientations. The kinetic energy operator in Eq. 2 depends quadratically on π_i and therefore both linearly and quadratically on \mathbf{B} . For the field strengths considered here, on the order of $B_0 = 2.35 \times 10^5$ T (one atomic unit), the linear and quadratic field contributions to the Hamiltonian are equally important, resulting in a complicated chemistry in this regime.

To ensure gauge origin invariance, we expand the MOs linearly in a set of field-dependent atom-fixed Cartesian Gaussian atomic orbitals (AOs) of the form

$$\chi_{ijk}(\mathbf{r}, \mathbf{K}, \mathbf{B}, \mathbf{O}) = N_{ijk} x_K^i y_K^j z_K^k \times \exp\left[\frac{1}{2} i \mathbf{B} \times (\mathbf{O} - \mathbf{K}) \cdot \mathbf{r}\right] \exp(-a r_K^2) \quad (3)$$

where \mathbf{r} is the position of the electron relative to the origin of the coordinate system, \mathbf{r}_K is its

position relative to the center of the Gaussian \mathbf{K} (here an atomic center), $a > 0$ is the Gaussian exponent, and N_{ijk} is the normalization constant. These AOs depend on the field \mathbf{B} and on the gauge origin \mathbf{O} in a physically reasonable manner, being correct to first order in the external magnetic field and ensuring gauge origin invariance of all computed expectation values. The use of such field-dependent orbitals, introduced by London in 1937 (15), is a standard technique in perturbative treatments of molecular magnetic phenomena (16–19). The use of London orbitals in nonperturbative studies is technically more complicated and therefore uncommon. Indeed, London orbitals have previously been used only in calculations on the one-electron H_2^+ molecule (20–22), on the two-electron H_2 molecule (6, 7), and on larger molecules by our group (23, 24), all at the uncorrelated Hartree-Fock level of theory [see also the Heitler-London model of Basile *et al.* (9)]. Our gauge origin-invariant FCI code allows us to study molecules in different electronic states and arbitrary orientations in a reliable

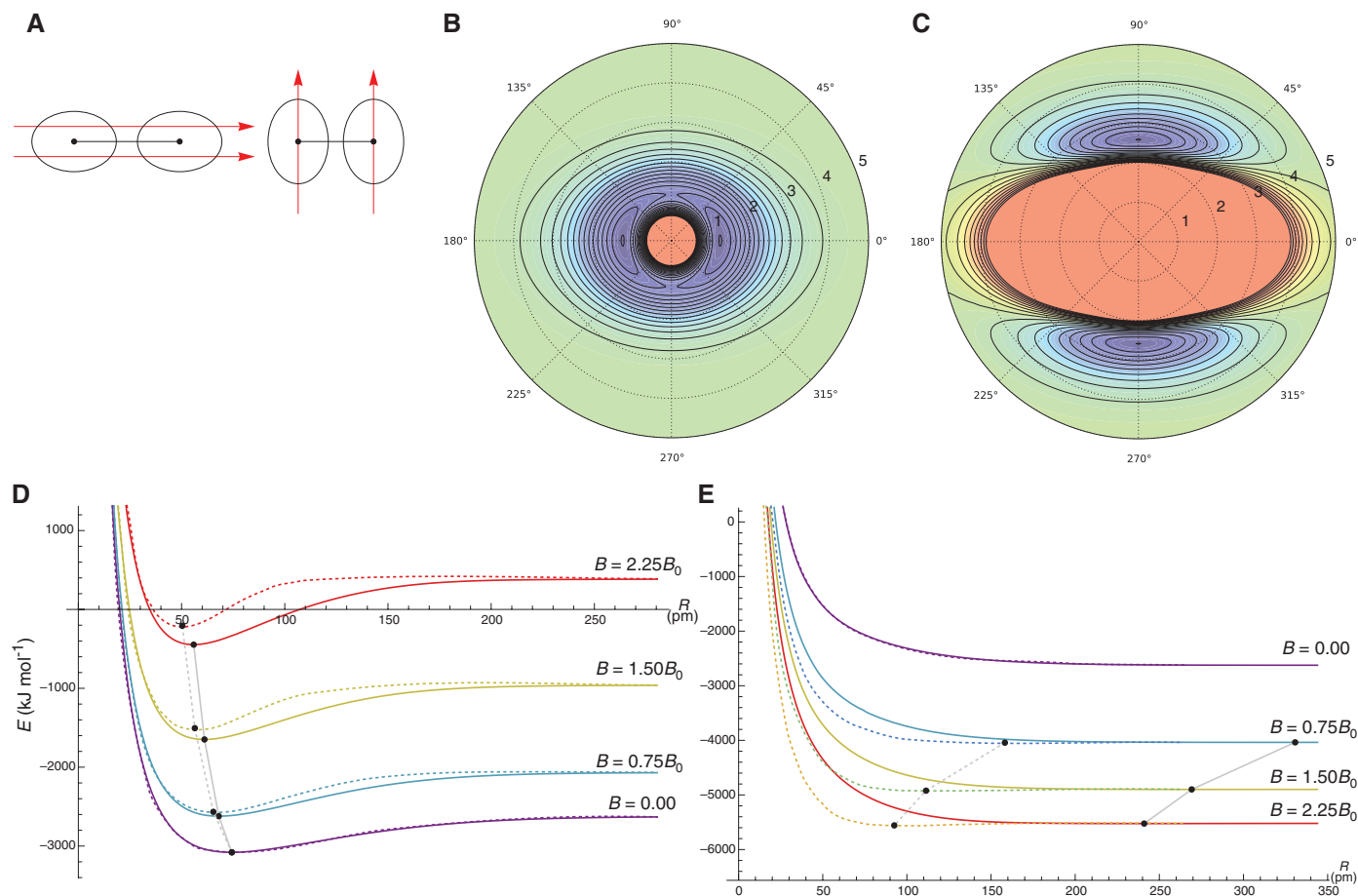


Fig. 1. The H_2 molecule in an external magnetic field. **(A)** Schematic illustration of the chemical bonding in parallel orientation (left) and perpendicular orientation (right) relative to the magnetic field, represented by red arrows. **(B and C)** Potential energy surfaces $E(R, \theta)$ of H_2 in the $1\Sigma_g^+(1\sigma_g^2)$ state (B) and the $3\Sigma_u^+(1\sigma_g 1\sigma_u^*)$ state (C) calculated at the FCI/un-aug-cc-pVTZ level of theory in a field of strength $B = 1.0B_0$, using a polar coordinate system where R is the internuclear separation and θ is the angle of the molecular

axis relative to the field (high values in red, low values in blue). **(D and E)** Potential energy curves $E(R, \theta)$ of the $1\Sigma_g^+(1\sigma_g^2)$ state (D) and the $3\Sigma_u^+(1\sigma_g 1\sigma_u^*)$ state (E) calculated at different field strengths in parallel orientation ($\theta = 0^\circ$, solid lines) and perpendicular orientation ($\theta = 90^\circ$, dashed lines). The areas between the full and dashed lines represent the energy for intermediate (skew) orientations in the field. The minimum of each curve is marked with a black dot.

and unbiased manner. A more flexible but computationally demanding scheme has been proposed by Kennedy and Kobe, who equipped the wave function with a variationally optimized phase factor (25).

In all calculations reported here, we use the correlation-consistent aug-cc-pVTZ basis set (26, 27) in uncontracted form (denoted un-aug-cc-pVTZ). For B on the order of or greater than B_0 , the anisotropic distortion of the electronic distribution by the magnetic field is most economically described using anisotropic AOs, with different Gaussian exponents in the parallel and perpendicular directions relative to the field (28, 29). The isotropic un-aug-cc-pVTZ basis that we use is sufficient for an accurate description of electronic systems in fields up to B_0 but becomes progressively less suited in stronger fields, as the systems become more compact and anisotropic. Selected FCI calculations carried out in the larger un-aug-cc-pVQZ basis and in the un-aug-cc-pVTZ basis with extra orbitals added confirm that the un-aug-cc-pVTZ basis provides a qualitatively correct description of the systems studied here.

Because of the shrinking prolate shape of the constituent atoms, diatomic molecules become smaller and develop an energy dependence on

their orientation in a magnetic field, as illustrated for the parallel and perpendicular orientations in Fig. 1A. In the covalently bound singlet state, the electronic energy of H_2 increases diamagnetically with increasing field strength (Fig. 1D). Moreover, the molecule becomes shorter and more strongly bound, reflecting a more pronounced diamagnetic behavior in the dissociation limit than in the united-atom limit. As expected for a covalently bound state, the energy is lower in the parallel orientation than in the perpendicular orientation (Fig. 1A), owing to the greater interatomic overlap in this orientation. In the polar plot for $B = B_0$ (Fig. 1B), we therefore observe global minima at inclination angles $\theta = 0^\circ, 180^\circ$ connected by saddle points at $\theta = 90^\circ, 270^\circ$. As the field increases from 0 to $2.25B_0$ (the strongest field considered here), the bond distance R_e decreases by 24% from 74 to 56 pm, while the dissociation energy D_e (without the zero-point vibrational contribution) increases by 83%, from 455 kJ mol $^{-1}$ to 834 kJ mol $^{-1}$. Because of the prolate shape of the atoms, the saddle points for rotation occur at a slightly shorter distance of 50 pm, with a barrier to rotation of 239 kJ mol $^{-1}$.

The triplet state $^3\Sigma_u^+(1\sigma_g 1\sigma_u^*)$ behaves very differently from the singlet state. With increasing field strength, the energy of the $\beta\beta$ triplet com-

ponent in Fig. 1E (the ground state for all finite fields considered here) is lowered paramagnetically and the system becomes more compact, as expected from the shrinking atomic size. The molecule thereby becomes bound, with a preferred perpendicular orientation in the field. At $B = 2.25B_0$, for instance, the bond distance is 92 pm and the dissociation energy 38 kJ mol $^{-1}$. The barrier to rotation is only slightly lower, 34 kJ mol $^{-1}$, with saddle points at a large internuclear separation of 241 pm. The other two triplet components behave in the same manner but with the energy shifted upward by the Zeeman interaction. The different shapes of the H_2 singlet and triplet surfaces are immediately apparent from the polar plots in Fig. 1, B and C. Although both surfaces are distinctively prolate in the field direction, the plots reveal two very different states: a fairly isotropic, compact singlet state with parallel global minima connected by perpendicular saddle points, contrasted with a more anisotropic, diffuse triplet state with a larger inaccessible inner region and perpendicular minima connected by parallel saddle points.

To understand the mechanism responsible for the field-induced perpendicular bonding, we examine the behavior of the bonding $1\sigma_g$ and antibonding $1\sigma_u^*$ orbitals in an external magnetic

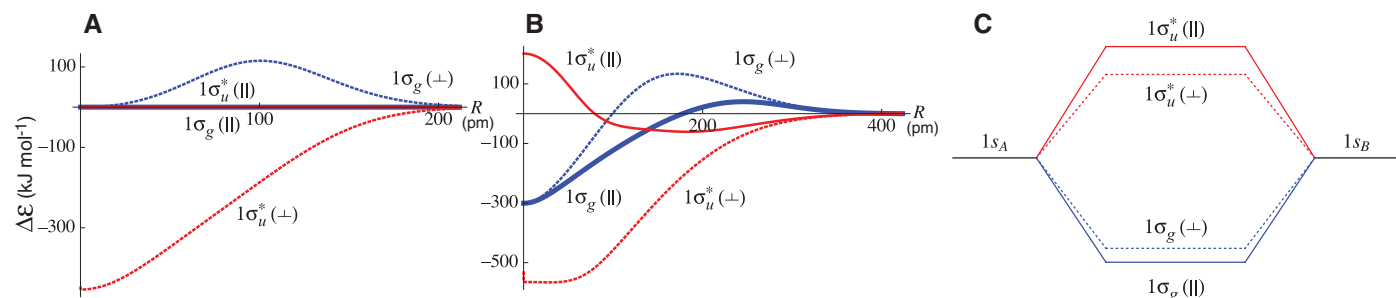


Fig. 2. Orbital energies of the bonding $1\sigma_g$ (blue) and antibonding $1\sigma_u^*$ (red) H_2 orbitals in parallel orientation (solid lines) and perpendicular orientation (dashed lines) relative to an external magnetic field. **(A)** The field-induced change in the orbital bonding energy $\Delta\mathcal{E}_p(R, \theta, B_0)$ calculated with a fixed

exponent $a = 1$ for different internuclear separations R . **(B)** The field-induced change in the orbital bonding energy $\Delta\mathcal{E}_p(R, \theta, B_0)$ calculated with an optimized exponent for different internuclear separations R . **(C)** The MO energy level diagram in a magnetic field.

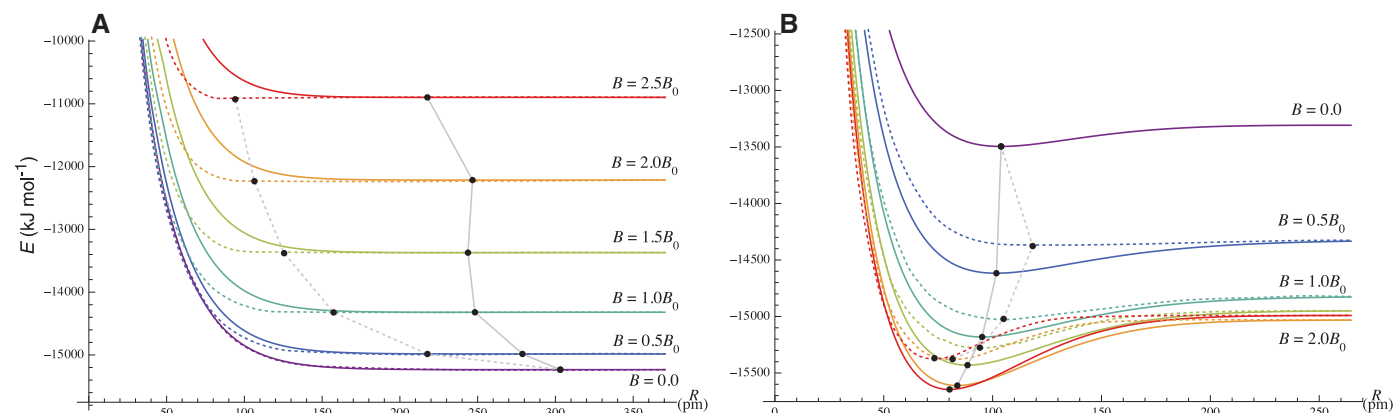


Fig. 3. **(A)** Potential energy curve of He_2 in the $^1\Sigma_g^+(1\sigma_g^2 1\sigma_u^{*2})$ state calculated using FCI/un-aug-cc-pVTZ theory in parallel orientation (solid lines) and perpendicular orientation (dashed lines) for $0 \leq B \leq 2.5B_0$. **(B)** Same as **(A)** for He_2 in the $^3\Sigma_u^+(1\sigma_g 1\sigma_u^* 2\sigma_g)$ state. The energy minimum of each curve is marked with a black dot.

field. In a minimal basis consisting of two 1s Gaussian orbitals of the form given in Eq. 3 with $i = j = k = 0$, the normalized bonding and antibonding MOs of H_2 located on the z axis in an external field \mathbf{B} of arbitrary orientation are given by

$$1\sigma_{g/u} = \left\{ 2 \pm 2 \exp\left[-\frac{a}{2}(1 + \tilde{B}_x^2 + \tilde{B}_y^2)R^2\right]\right\}^{-1/2} \times (1s_A \pm 1s_B) \quad (4)$$

where $1s_A$ and $1s_B$ are 1s orbitals with exponent a on the two atoms, R is the internuclear separation, and $\tilde{B}_x = B_x/4a$ and $\tilde{B}_y = B_y/4a$ are scaled perpendicular field components. There is no contribution from B_z to the MOs. When R tends to zero, these MOs transform smoothly into helium AOs of the same exponent:

$$\lim_{R \rightarrow 0} 1\sigma_g = 1s \quad (5)$$

$$\lim_{R \rightarrow 0} 1\sigma_u^* = (1 + \tilde{B}_x^2 + \tilde{B}_y^2)^{-1/2} \times (2p_z + i\tilde{B}_x 2p_y - i\tilde{B}_y 2p_x) \quad (6)$$

Whereas $1\sigma_g$ transforms into an 1s orbital, $1\sigma_u^*$ transforms into a combination of 2p orbitals. In particular, for $\tilde{B} = 1$, $1\sigma_u^*$ becomes $2p_0$ in the parallel orientation and $2p_{-1}$ in the perpendicular orientation. In a magnetic field, the $2p_{-1}$ orbital has a lower energy than the $2p_0$ orbital (by the orbital-Zeeman interaction); therefore, $1\sigma_u^*$ favors a perpendicular orientation relative to the magnetic field. No such orientational preference is observed for $1\sigma_g$, which transforms into the same 1s orbital in all orientations. By this argument, H_2 adopts a perpendicular orientation in the triplet state, with its singly occupied bonding and antibonding orbitals.

Let $\mathcal{E}_p(R, \theta, B)$ be the orbital energy of ϕ_p at configuration (R, θ) and in the field B , and consider the quantity

$$\Delta\mathcal{E}_p(R, \theta, B) = [\mathcal{E}_p(R, \theta, B) - \mathcal{E}_p(R, \theta, 0)] - [\mathcal{E}_p(\infty, \theta, B) - \mathcal{E}_p(\infty, \theta, 0)] \quad (7)$$

which represents the field-induced change in the orbital energy $\mathcal{E}_p(R, \theta, B) - \mathcal{E}_p(R, \theta, 0)$ at

the molecular configuration (R, θ) relative to the change observed in the dissociation limit. With a fixed orbital exponent $a = 1$, we observe the expected stabilization of $1\sigma_u^*$ in the perpendicular orientation (and a smaller $1\sigma_g$ destabilization in the bonding region), and neither stabilization nor destabilization in the parallel orientation (Fig. 2A). However, when the exponent a is variationally optimized for each (R, θ) (Fig. 2B), $1\sigma_g$ is stabilized in the united atom (where the orientation no longer matters for this orbital), whereas $1\sigma_u^*$ (for which the orientation in the united atom matters) is destabilized in the parallel orientation but further stabilized in the perpendicular orientation. These changes lead to the modified MO energy level diagram shown in Fig. 2C and to the following energy ordering of the lowest H_2 states in a magnetic field:

$$E_{\parallel}(1\sigma_g^2) \leq E_{\perp}(1\sigma_g^2) \leq E_{\perp}(1\sigma_g 1\sigma_u^*) \leq E_{\parallel}(1\sigma_g 1\sigma_u^*) \quad (8)$$

The field-induced bonding of H_2 in the perpendicular orientation is thus not covalent in nature, nor does it depend on dispersion. Instead, it arises from a lowering (relative to the atomic limit) of the kinetic energy associated with the induced paramagnetic rotation of the electron in the antibonding orbital. The pivotal role of the kinetic energy is confirmed by FCI calculations on H_2 ; although the field-induced changes in the FCI kinetic and electrostatic energies at a given (R, θ) are of the same order of magnitude, the appearance of a minimum in the dissociation curve is almost entirely due to the lowering of the kinetic energy.

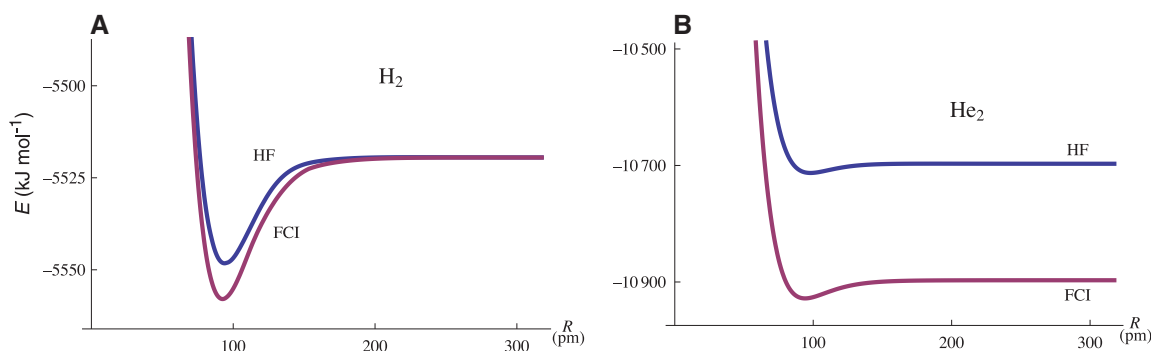
As shown in Fig. 2, the bonding $1\sigma_g$ orbital favors a perpendicular orientation in a magnetic field for intermediate bond distances. In general, therefore, the orientation of H_2 in the triplet state depends on a balance between the preference of $1\sigma_g$ for a parallel orientation and the preference of $1\sigma_u^*$ for a perpendicular orientation. Indeed, for $B = 2.25B_0$, the H_2 minimum shifts slightly away from the perpendicular orientation. Eventually, the H_2 ground state changes from ${}^3\Sigma_u^+(1\sigma_g 1\sigma_u^*)$ to ${}^3\Pi_u(1\sigma_g 1\pi_u)$, which is covalently bound with a

preferred parallel field orientation, as observed by Kubo using Hartree-Fock theory (7).

To demonstrate that the behavior observed for H_2 is a general phenomenon, we have calculated the potential energy curves of He_2 in its lowest ${}^1\Sigma_u^+(1\sigma_g^2 1\sigma_u^{*2})$ singlet (Fig. 3A) and ${}^3\Sigma_u^+(1\sigma_g^2 1\sigma_u^{*2} 2\sigma_g)$ triplet (Fig. 3B) states. Without a field, the He_2 singlet ground state is weakly bound by dispersion, with $R_e = 297$ pm and $D_e = 0.092$ kJ mol $^{-1}$ (30). In the field, the energy increases diamagnetically. Moreover, He_2 assumes a perpendicular orientation, becoming smaller and more strongly bound, with a bond distance of 94 pm and a dissociation energy of 31 kJ mol $^{-1}$ at $B = 2.5B_0$. The nonmonotonic variation of the saddle point (in the parallel orientation) may be an artifact arising from basis set incompleteness. In the triplet state, the covalently bound He_2 molecule behaves similarly to H_2 in the singlet state. As the field increases to $2.5B_0$, the molecule aligns with the field and shortens from 104 pm to 80 pm while the dissociation energy increases from 178 kJ mol $^{-1}$ to 655 kJ mol $^{-1}$. In the $\beta\beta$ component of the triplet, He_2 becomes diamagnetic at $B \approx 2.2B_0$.

We have presented advanced FCI calculations on H_2 and He_2 in strong magnetic fields and explained their behavior in terms of elementary concepts of MO theory. To examine the role of electron correlation, we compare the FCI and Hartree-Fock potential energy curves of triplet H_2 (Fig. 4A) and singlet He_2 (Fig. 4B). These plots demonstrate that the paramagnetic perpendicular bonding discussed above does not require electron correlation for its qualitative description; Hartree-Fock theory, in which electronic interactions are described in an averaged, mean-field manner, recovers all the main effects of paramagnetic bonding, underestimating the bond distance slightly and the dissociation energy more strongly. The bonding is clearly not van der Waals in nature, although electron correlation is necessary for its quantitative description. In short, we have identified a distinct mechanism for chemical bonding in strong magnetic fields, arising from the stabilization of antibonding orbitals in a perpendicular orientation relative to the magnetic field. This stabilization leads to the bonding of

Fig. 4. (A) The FCI and unrestricted Hartree-Fock (HF) dissociation curves of H_2 in the ${}^3\Sigma_u^+(1\sigma_g 1\sigma_u^*)$ state for $B_{\perp} = 2.25B_0$ calculated in the un-aug-cc-pVTZ basis set. (B) Same as (A) for He_2 in the ${}^1\Sigma_g^+(1\sigma_g^2 1\sigma_u^{*2})$ state for $B_{\perp} = 2.5B_0$. The Hartree-Fock model overestimates the bond distances of H_2 and He_2 by 1.5 and 4.1%, respectively, whereas the dissociation energies are underestimated by 25 and 49%. The counterpoise corrections for the basis-set superposition error (not added to the plotted curves) are 4 kJ mol $^{-1}$ and 2 kJ mol $^{-1}$, respectively, for H_2 and He_2 at the equilibrium distances.



species of zero bond order, which are either unbound or bound by dispersion in the absence of a magnetic field. This bonding is sufficiently strong to affect the chemistry of molecules in strong magnetic fields.

References and Notes

1. T. Helgaker, W. Klopper, D. P. Tew, *Mol. Phys.* **106**, 2107 (2008).
2. R. H. Garstang, *Rep. Prog. Phys.* **40**, 105 (1977).
3. S. Jordan, P. Schmelcher, W. Becken, W. Schweizer, *Astron. Astrophys.* **336**, L33 (1998).
4. S. Jordan, P. Schmelcher, W. Becken, *Astron. Astrophys.* **376**, 614 (2001).
5. D. Lai, *Rev. Mod. Phys.* **73**, 629 (2001).
6. M. Zaucer, A. Ažman, *Phys. Rev. A* **18**, 1320 (1978).
7. A. Kubo, *J. Phys. Chem. A* **111**, 5572 (2007).
8. Y. E. Lozovik, A. V. Klyuchnik, *Phys. Lett. A* **66**, 282 (1978).
9. S. Basile, F. Trombetta, G. Ferrante, *Nuovo Cim.* **9**, 457 (1987).

10. P. J. Knowles, N. C. Handy, *Chem. Phys. Lett.* **111**, 315 (1984).
11. W. Duch, *GRMS or Graphical Representation of Model Spaces I: Basics* (Springer-Verlag, New York, 1986).
12. J. Olsen, B. O. Roos, P. Jørgensen, H. J. A. Jensen, *J. Chem. Phys.* **89**, 2185 (1988).
13. T. Helgaker, P. Jørgensen, J. Olsen, *Molecular Electronic-Structure Theory* (Wiley, Chichester, UK, 2000).
14. P. Schmelcher, L. S. Cederbaum, *Phys. Rev. A* **41**, 4936 (1990).
15. F. London, *J. Phys. Radium* **8**, 397 (1937).
16. R. Ditchfield, *J. Chem. Phys.* **56**, 5688 (1972).
17. K. Wolinski, J. F. Hinton, P. Pulay, *J. Am. Chem. Phys. Soc.* **112**, 8251 (1990).
18. W. Kutzelnigg, *Isr. J. Chem.* **19**, 193 (1980).
19. M. Schindler, W. Kutzelnigg, *J. Chem. Phys.* **76**, 1919 (1982).
20. U. Kappes, P. Schmelcher, *Phys. Lett. A* **210**, 409 (1996).
21. U. Kappes, P. Schmelcher, *Phys. Rev. A* **53**, 3869 (1996).
22. U. Kappes, P. Schmelcher, *Phys. Rev. A* **54**, 1313 (1996).
23. E. I. Tellgren, A. Soncini, T. Helgaker, *J. Chem. Phys.* **129**, 154114 (2008).

24. E. I. Tellgren, T. Helgaker, A. Soncini, *Phys. Chem. Chem. Phys.* **11**, 5489 (2009).
25. P. K. Kennedy, D. H. Kobe, *Phys. Rev. A* **30**, 51 (1984).
26. T. H. Dunning, *J. Chem. Phys.* **90**, 1007 (1989).
27. D. E. Woon, T. H. Dunning, *J. Chem. Phys.* **100**, 2975 (1994).
28. P. Schmelcher, L. S. Cederbaum, *Phys. Rev. A* **37**, 672 (1988).
29. U. Kappes, P. Schmelcher, *J. Chem. Phys.* **100**, 2878 (1994).
30. M. Jeziorska, W. Cencek, K. Patkowski, B. Jeziorski, K. Szalewicz, *J. Chem. Phys.* **127**, 124303 (2007).

Acknowledgments: Supported by the Norwegian Research Council through Centre for Theoretical and Computational Chemistry (CTCC) grant 179568/V30 and through grant 197446/V30 and by the European Research Council (ERC) under the European Union's Seventh Framework Program through the advanced grant ABACUS, ERC grant agreement 267683. M.R.H. acknowledges support from the CTCC during a sabbatical stay at the University of Oslo in 2010.

26 January 2012; accepted 25 May 2012
10.1126/science.1219703

Sulfate Burial Constraints on the Phanerozoic Sulfur Cycle

Itay Halevy,^{1,2*} Shanan E. Peters,³ Woodward W. Fischer²

The sulfur cycle influences the respiration of sedimentary organic matter, the oxidation state of the atmosphere and oceans, and the composition of seawater. However, the factors governing the major sulfur fluxes between seawater and sedimentary reservoirs remain incompletely understood. Using macrostratigraphic data, we quantified sulfate evaporite burial fluxes through Phanerozoic time. Approximately half of the modern riverine sulfate flux comes from weathering of recently deposited evaporites. Rates of sulfate burial are unsteady and linked to changes in the area of marine environments suitable for evaporite formation and preservation. By contrast, rates of pyrite burial and weathering are higher, less variable, and largely balanced, highlighting a greater role of the sulfur cycle in regulating atmospheric oxygen.

Sulfate (SO_4^{2-}) is the fourth most abundant ion in modern seawater and a major component of the alkalinity budget, which governs the pH of seawater (1). Bacterial sulfate reduction accounts for ~50% of sedimentary organic matter respiration (2), and precipitation of pyrite (FeS_2) is one of the major exit channels of sulfur from the ocean (3). Because reduction of riverine sulfate and burial of the sulfide leave oxidized products in the ocean-atmosphere system, pyrite burial is considered a major indirect source of oxygen to the atmosphere (4, 5).

Several time series data sets constrain aspects of the Phanerozoic sulfur cycle (Fig. 1A). The sulfur isotope composition, $\delta^{34}\text{S}$, of carbonate-associated sulfate, sulfate evaporites, and barite (BaSO_4) records the $\delta^{34}\text{S}$ of seawater sulfate, whereas the $\delta^{34}\text{S}$ of sedimentary pyrite captures the products of microbial sulfate reduction (6–8).

¹Environmental Sciences and Energy Research, Weizmann Institute of Science, Rehovot 76100, Israel. ²Geological and Planetary Sciences, California Institute of Technology, Pasadena, CA 91125, USA. ³Geoscience, University of Wisconsin-Madison, Madison, WI 53706, USA.

*To whom correspondence should be addressed. E-mail: itay.halevy@weizmann.ac.il

The chemical composition of fluid inclusions in halite constrains the concentration of major ions in seawater, including sulfate (9, 10).

Variability in the $\delta^{34}\text{S}$ records of seawater sulfate and sedimentary pyrite is typically interpreted to reflect changes in the fraction of sulfur removed from the oceans as pyrite, f_{pyr} . Because pyrite is depleted in ^{34}S by several percent relative to the sulfate reservoir from which it formed, times of high seawater sulfate $\delta^{34}\text{S}$ are interpreted as times of high rates of pyrite burial. By assuming a steady state and constant input magnitude and $\delta^{34}\text{S}$, or by scaling inputs and outputs to modern values, models of the Phanerozoic sulfur cycle explain long-term trends in $\delta^{34}\text{S}$ values by changes in f_{pyr} between ~0.2 and ~0.6 (4, 11–13). Recognizing that the magnitude and $\delta^{34}\text{S}$ of the influxes to the ocean have likely varied in time, thereby influencing the isotopic record, some models included parameterized influxes and solved mass balance equations for the outfluxes and the value of f_{pyr} (4, 13). The parameterizations are uncertain, however, because they are largely based on a scaling of modern influxes by debated factors, such as the relative rates of seafloor spreading and continental runoff (14, 15).

It is possible to measure the sink of sulfate evaporites from seawater and obtain estimates of the influx magnitude and $\delta^{34}\text{S}$ by mass balance, though previous volume estimates of Phanerozoic evaporites (mostly halite, but some sulfate) have been considered too coarse or uncertain to accurately constrain past rates of sulfate burial (16–18). We quantified sulfate burial over Phanerozoic time, using a comprehensive macrostratigraphic database (19, 20), which includes 23,843 lithostratigraphic rock units in 949 geographic locations across North America and the Caribbean (NAC). Data were binned by age, and sulfate burial rates were obtained by dividing evaporite volume by bin duration. Macrostratigraphy-based estimates of sulfate burial rates are higher than those derived from other compilations. This is due to the improved spatial and lithological resolution of this data set, which includes sedimentary rocks in the surface and subsurface, and many comparatively thin but widespread deposits not included in previous compilations. Notably, the NAC burial rates are highly variable, with values 2 to 14 times the average occurring mainly in Paleozoic intervals (Fig. 1C).

The macrostratigraphic database currently provides comprehensive coverage only in NAC, but can be scaled globally (Fig. 1D) by using mechanistic relationships between the observations and environmental controls on sulfate evaporite deposition (20). The volume-weighted average ratio of global to North American sulfate deposit volumes is ~8 (16, 17). In comparison, the area-weighted ratio of global to NAC submerged continental area in latitudes of net evaporation, estimated from paleogeographic reconstructions (20, 21), is ~7. This close agreement reflects a primary requirement for massive sulfate evaporite deposition—hydrographic isolation of large, marine-fed basins at latitudes of net evaporation (22). Such basins are created by rifting, small changes in sea level or the development of a barrier to circulation (22), often at the shoreward edge of submerged continental shelves. Indeed,